ANL-23/60

Argonne NATIONAL LABORATORY

Advanced Turbulence Models for Large-Scale Atmospheric Boundary Layer Flows

Mathematics and Computer Science

ANL-23/60

Advanced Turbulence Models for Large-Scale Atmospheric Boundary Layer Flows

prepared by

Ananias Tombouldies[2], Misun Min[1,*], Paul Fischer[1,3,4], Matt Churchfield[5], Michael Sprague[5]

[1] Mathematics and Computer Science Division, Argonne National Laboratory
[2] Department of Mechanical Engineering, Aristotle University of Thessaloniki
[3] Department of Computer Science, University of Illinois Urbana-Champaign
[4] Mechanical Science & Engineering, University of Illinois Urbana-Champaign
[5] National Wind Technology Center, National Renewable Energy Laboratory
* corresponding author

September 28, 2023

Contents

Executive Summary

We present high-fidelity large-eddy-simulation modeling approaches for the turbulent atmospheric boundary layer flows. Wind energy is a prime example of an application driven by the atmospheric boundary layer. Generation of electrical energy from farms of wind turbines at night in the stable atmospheric boundary layer is a particularly interesting situation. In this report, we consider the well-known Global Energy and Water Cycle Experiment-Atmospheric Boundary Layer Study (GABLS) stably stratified benchmark large-eddy simulation case. We use a high-order spectral element code Nek5000/RS, which is supported under the U.S. Department of Energy's Exascale Computing Project Center for Efficient Exascale Discretizations project, targeting application simulations on various acceleration-device-based exascale computing platforms [1, 2, 3]. In our earlier Argonne National Laboratory report [4], we demonstrated our newly developed subgrid-scale models based on high-pass filter, mean-field eddy viscosity, and Smagorinsky with no-slip and traction boundary conditions, provided with low-order statistics, convergence, and turbulent structure analysis. In this report, we extend the range of our subgrid-scale modeling approaches in the context of the mean-field eddy viscosity [5] to include the solution of a subgrid-scale turbulent kinetic energy equation. We demonstrate the model fidelity of Nek5000/RS in comparison to that of AMR-Wind, a block-structured second-order finite-volume code with adaptive-mesh-refinement capabilities, with which we studied and compared scaling performance of both codes on the U.S. Department of Energy's leadership computing platforms [6].

1 Introduction

Atmospheric boundary layer (ABL) flows are turbulent, and the state of the turbulence is affected by density stratification that arises in large part from surface heating and cooling. Additionally, Coriolis effects caused by planetary rotation and curvature complicate the flow. Furthermore, regional-scale weather patterns and terrain add complexity to the ABL. Significant research effort is applied to ABL flows because of their importance and complexity [7, 8, 9]. This work focuses on numerical computation of ABL flows using large-eddy simulation (LES), where the governing physics equations are solved in filtered form such that the larger, energy-containing eddies are directly resolved and the remaining "subgrid-scale" (SGS) turbulence is modeled.

The ABL community has set up a sequence of benchmark problems, the GEWEX (Global Energy and Water Cycle Experiment) Atmospheric Boundary Layer Study (GABLS) [10] to quantify the effects of numerical modeling and discretization choices. These benchmarks represent the atmospheric boundary layer in regional and large-scale atmospheric models and are considered important benchmarks for improving modeling approaches for the study of wind energy, climate, and weather on all scales [11].

In this report, we consider the GABLS1 benchmark, illustrated in Figure 1, which is a well-documented stably stratified flow problem. The studies are conducted using the Argonne-developed open-source Navier–Stokes solver, Nek5000/RS, which is based on high-order spectral element discretizations [12]. NekRS [1] is a GPU-accelerated version of Nek5000 [13] developed under the DOE's Exascale Computing Project (ECP) Center for Efficient Exascale Discretizations (CEED) project [14], targeting application simulations on various acceleration-device-based exascale computing platforms [1, 2].

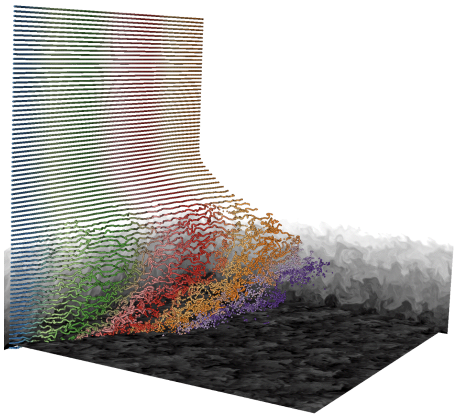

Figure 1: NekRS simulation for the atmospheric boundary layer flows demonstrating the potential temperature on the vertical planes and the streamwise velocity on the horizontal plane.

In our earlier ANL report [4], we demonstrated our newly developed subgrid-scale (SGS) models based on high-pass filter (HPF), mean-field eddy viscosity (MFEV), and Smagorinsky (SMG) with no-slip and traction boundary conditions, provided with low-order statistics, convergence, and turbulent structure analysis. In this report, we extend the range of our SGS modeling approaches in the context of MFEV [5], to include the solution of an SGS turbulent kinetic energy (TKE) equation. The model fidelity and scaling performance of Nek5000/RS on DOE's leadership computing platforms in comparison to those of AMR-Wind, a block-structured second-order finite-volume code with adaptive-mesh-refinement capabilities, were discussed in [6]. Here, we demonstrate the model fidelity of Nek5000/RS in comparison to that of AMR-Wind.

This report is organized as follows: Section 2 presents the governing equations for our LES modeling approach. Section 3 describes the benchmark problem and discusses our SGS models, validation, and convergence studies. Section 4 demonstrates the results obtained with the newly implemented SGS models. Section 5 concludes.

2 Large-Eddy Simulation Model

For the atmospheric LES, we consider the governing equations consisting of the incompressible Navier–Stokes and potential temperature equations in nondimensional form, solved in a *spatially filtered* resolved-scale formulation defined as

$$\frac{\partial \bar{u}_i}{\partial t} + \bar{u}_j \frac{\partial \bar{u}_i}{\partial x_j} = -\frac{1}{\bar{\rho}} \frac{\partial \bar{p}}{\partial x_i} - \frac{\partial \tau_{ij}}{\partial x_j} + f_i - \frac{\theta'}{\theta_0} g_i, \tag{1}$$

$$\frac{\partial \bar{u}_j}{\partial x_j} = 0, \tag{2}$$

$$\frac{\partial \bar{\theta}}{\partial t} + \bar{u}_j \frac{\partial \bar{\theta}}{\partial x_j} = -\frac{\partial \tau_{\theta j}}{\partial x_j}, \tag{3}$$

where $\bar{u}_i$ is the ith component of the resolved-scale velocity vector, $\bar{\rho}$ is the density, $\bar{p}$ is the pressure, g_i is the gravity acceleration vector, and $\bar{\theta}$ is the resolved-scale potential temperature. The scalar θ'/θ_0 is the buoyancy force defined by

$$\frac{\theta'}{\theta_0} = \frac{\bar{\theta} - \theta_0}{\theta_0}, \tag{4}$$

where θ_0 is the reference potential temperature. f_i represents the Coriolis acceleration defined by

$$f_i = -2\epsilon_{ijk}\Omega_j \bar{u}_k, \tag{5}$$

where ϵ_{ijk} is the alternating tensor, Ω_j is the planetary rotation rate vector at the point of interest on the planet (which is dependent on latitude).

In addition, τ_{ij} and $\tau_{\theta j}$ are the stress tensors in the momentum and energy equations including subgrid-scale (SGS) modeling terms defined as

$$\tau_{ij} = -\frac{2}{Re} S_{ij} + \tau_{ij}^{sgs} = -\frac{1}{Re}\left(\frac{\partial \bar{u}_i}{\partial x_j} + \frac{\partial \bar{u}_j}{\partial x_i}\right) + \tau_{ij}^{sgs}, \tag{6}$$

and

$$\tau_{\theta j} = -\frac{1}{Pe} \frac{\partial \bar{\theta}}{\partial x_j} + \tau_{\theta j}^{sgs}, \tag{7}$$

where Re is the Reynolds number, Pe is the Peclet number, S_{ij} is the resolved-scale strain-rate tensor, and τ_{ij}^{sgs} and $\tau_{\theta j}^{sgs}$ are the subgrid scale stress tensors.

3 Benchmark Cases and Modeling Approaches

We consider the GABLS benchmark problem [15], which is a stable ABL in which the ground temperature is cooler than the air temperature and continues to cool over the duration of the simulation. We investigate several SGS modeling approaches and wall boundary conditions as discussed below.

3.1 ABL GABLS Benchmark

We describe the GABLS benchmark problem [15], a stable ABL in which the ground temperature (at $z = 0$) is cooler than the air temperature and continues to cool over the duration of the simulation. We define the domain as spanning $L_x \times L_y \times L_z = 400$ m $\times$ 400 m $\times$ 400 m, with the streamwise direction x, the spanwise direction y, and the vertical direction z. We initialize our simulations at time $t = 0$ with a constant velocity in the streamwise direction equal to the geostrophic wind speed of $U = 8$ m/s. We define the initial potential temperature by 265 K in $0 \leq z \leq 100$ m and linearly increase at a rate of 0.01 K/m in the range of 100 m $\leq z \leq 400$ m. The reference potential temperature is 263.5 K. The Reynolds number, defined as $Re = UL_b/\nu$, is approximately 50 million in this case, which precludes the use of direct numerical simulation wherein all turbulent scales are resolved. In estimating the Reynolds number, we use $L_b = 100$ m, which is the thickness of the initial thermal boundary layer, and ν is the molecular viscosity. We add an initial perturbation to the temperature with an amplitude of 0.1 K on the potential temperature field for $0 \leq z \leq 50$ m.

Periodic boundary conditions (BCs) are used in the streamwise and spanwise directions. At the top boundary ($z = 400$ m), a stress-free, rigid lid is applied for momentum, and the heat flux for the energy equation is set consistent with the 0.01 K/m temperature gradient initially prescribed in the upper region of the flow. At the bottom boundary, we perform simulations with impenetrable traction BCs for the velocity where the specified shear stress comes from Monin-Obukhov similarity theory [16]. For the energy equation, a heat flux is applied that is derived from the same theory and a specified potential temperature difference between the flow at a height, z_1, and the surface. The surface temperature is from the GABLS specification following the rule $\theta_b(t) = 265 - 0.25t$, where t is in hours. Because the boundary conditions are periodic (lateral), or the mass flow rate through the boundaries is zero (top and bottom), pressure boundary conditions are not needed.

3.2 SGS Modeling Approaches

We have extended the range of our SGS modeling approaches, in the context of the MFEV [5], to include the solution of an SGS TKE equation. In our earlier ANL report [4], we discussed the modeling approaches for the following:

(1) HPF SGS model + no-slip BCs
(2) HPF SGS model + traction BCs
(3) MFEV (SGS for anisotropic part) + HPF (SGS for isotropic) + traction BCs
(4) MFEV (SGS for anisotropic part) + SMG (SGS for isotropic) + traction BCs

In the earlier report [4], two different types of boundary conditions were used in Nek5000/NekRS at the bottom boundary representing the lower wall. These boundary conditions (BCs) were no-slip and traction BCs. In this report, we consider only traction boundary conditions for all simulations reported, in which the normal velocity component was forced to zero and traction BCs were specified for the two horizontal velocity components; in addition, heat flux BCs were specified for the potential temperature, based on the Monin-Obukhov log-law [16].

Results obtained with the MFEV/HPF approach led to converged results with increasing resolution. Figure 2 (a) shows horizontally averaged profiles of streamwise and spanwise velocities at $t = 7$ h, and demonstrates convergence with increasing resolution from $n = 128^3$ to $n = 1024^3$.

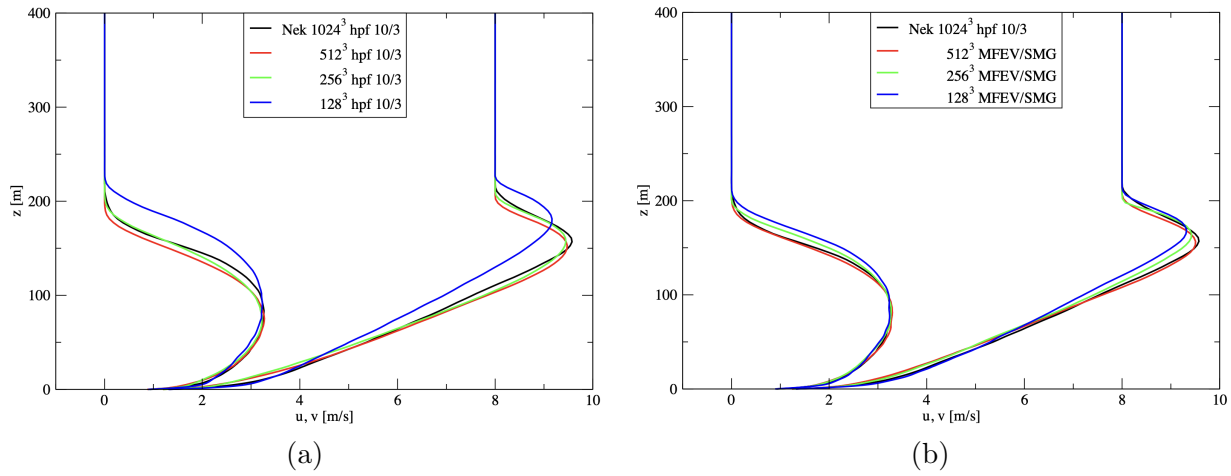

Figure 2: Nek5000 Convergence: (a) MEFV+HPF and (b) MFEV+SMG.

In addition, the obtained profiles were almost identical for different values of Re as well as of z_1^+ as reported in [4]. Results obtained with the MFEV/SMG approach also demonstrate convergence with increasing resolution as well as asymptotic convergence with Re and z_1^+. Moreover, convergence with resolution seems to be faster with MFEV/SMG as compared with the MFEV/HPF approach described earlier. This can be observed in Fig. 2 (b), which shows horizontally averaged streamwise and spanwise velocities at $t = 7$ h using MFEV/SMG and traction boundary conditions.

Interestingly, the difference between the mean profiles obtained with MFEV/HPF and MFEV/SMG is reduced with increasing resolution, as can be observed in Fig. 3 (a)–(c).

Figure 4 (a) shows the horizontally averaged streamwise and spanwise velocities and Fig. 4 (b) shows the horizontally averaged potential temperature at $t = 6$ h for the two highest resolutions 512^3 and 1024^3 for MFEV/HPF, and for 512^3 for MFEV/SMG and AMR-Wind. As can be observed, both Nek5000/NekRS converge to the same profiles as resolution is increased; they also agree well with the AMR-Wind obtained profiles at 512^3.

Figure 5 (a)–(d) show horizontally averaged streamwise and spanwise velocity profiles at different times $t = 6$ h, $t = 7$ h, $t = 8$ h, and $t = 9$ h, demonstrating good agreement between MFEV/HPF, MFEV/SMG, and AMR-Wind for $n = 512^3$.

Here, we focus primarily on the approaches that are based on an SGS TKE equation as follows:

(6) MFEV (SGS for anisotropic part) + SGS TKE (SGS for isotropic part) + L_{SMG}
(7) MFEV (SGS for anisotropic part) + SGS TKE (SGS for isotropic part) + L_{DRD}

The SGS TKE equation and the definition of the Smagorinsky and Deardorff length scales, L_{SMG} and L_{DRD}, respectively, are described below. In addition to the above, sampling for the evaluation of the wall momentum and heat fluxes was extended to include specified z-locations away from the lower wall.

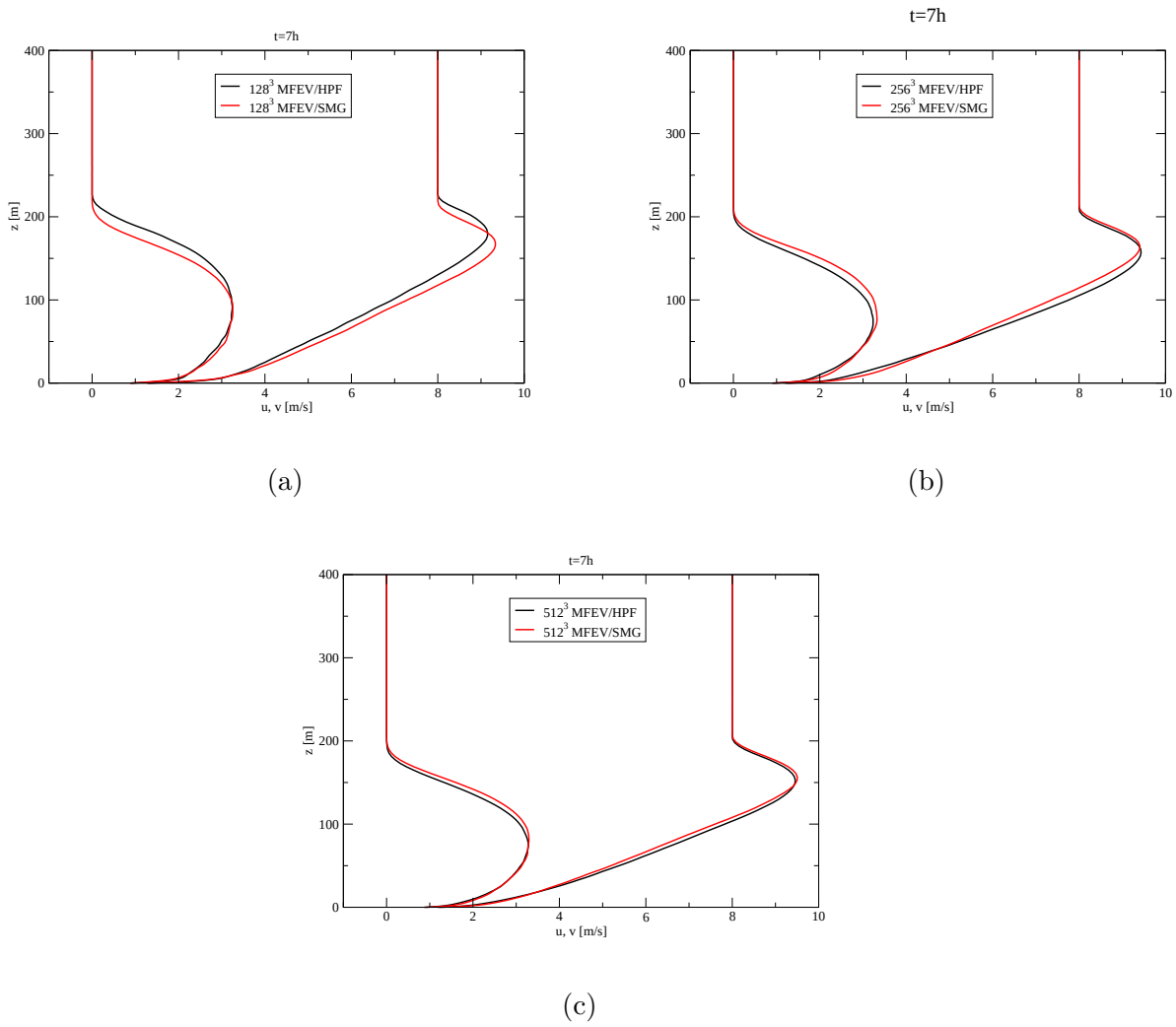

Figure 3: Comparison between mean profiles obtained with MEFV+HPF and MFEV+SMG with resolution (a) $n = 128^3$, (b) $n = 256^3$, and (c) $n = 512^3$.

MFEV (SGS for anisotropic part) + SGS TKE (SGS for isotropic) + traction BCs

In the efforts described in this subsection, the traction BCs for the horizontal velocity components are implemented in the context of the log-law for which we follow the approach of [17] and [18], which is suitable for finite element methods based on a weighted residual formulation. The normal component of the velocity is set to zero, and the traction BCs imposed on the tangential velocity are based on the horizontally averaged slip velocity that develops at the boundary or at a specified sampling z-location from the lower wall.

The SGS modeling is based on [5], where the SGS stress tensors τ_{ij}^{sgs} and $\tau_{\theta j}^{sgs}$ are expressed in terms of an anisotropic and an isotropic part. Thus, the SGS dissipation is based on an anisotropic,

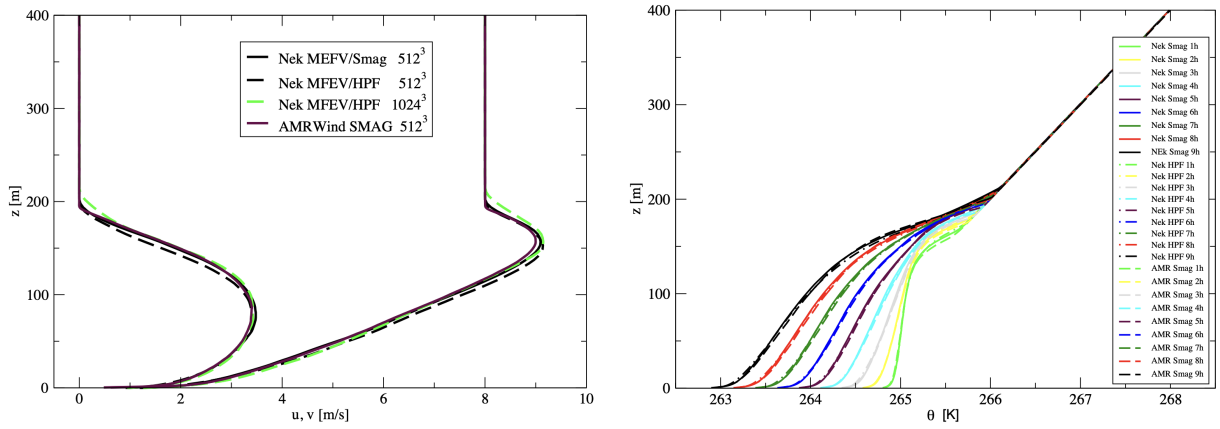

(a) (b)

Figure 4: Horizontally averaged (a) streamwise, spanwise velocities and (b) potential temperature at $t = 6$ h using MFEV/SMG and MFEV/HPF with traction boundary conditions, compared with AMR-Wind results, for 512^3.

MFEV ν_T obtained by the horizontally averaged mean strain rate, and an isotropic, fluctuating part ν_t, which is a function of the SGS TKE obtained from a transport equation as described below. The law of the wall is effected through the use of the MFEV concept, and the approach originally used by [19] is used to convert the horizontally averaged traction to local values based on the local slip velocity in each of the horizontal directions. The SGS model of [5] is based on the following expression

$$\tau_{ij}^{sgs} = -2\gamma\nu_t S_{ij} - 2\nu_T \langle S_{ij} \rangle , \tag{8}$$

where $\langle \ \rangle$ denote averaging over the homogeneous directions, and ν_T is an average eddy viscosity that is expressed in terms of mean flow quantities. In Eq. (8) γ is an "isotropy factor," which accounts for variability in the SGS constants due to anisotropy of the mean flow. The fluctuating eddy viscosity, ν_t, is obtained from the SGS turbulent kinetic energy equation, in which the shear production term is computed from the fluctuating velocities as suggested by [20]. When the fluctuating (isotropic) part of turbulent motion is taken into account through of the use the fluctuating strain rate, ν_t in Eq. (8) is non-zero and the full stress tensor has to be taken into account. Thus, the momentum and potential temperature equations are given by

$$\frac{\partial \bar{u}_i}{\partial t} + \bar{u}_j \frac{\partial \bar{u}_i}{\partial x_j} = -\frac{\partial \bar{p}}{\partial x_i} - \frac{\partial \tau_{ij}}{\partial x_j} - 2\epsilon_{i3k}\Omega\bar{u}_k + (1-\delta_{i3})\frac{\partial}{\partial z}\nu_T\frac{\partial\langle\bar{u}_i\rangle}{\partial z} - \frac{\theta'}{\theta_0}g_i \tag{9}$$

$$= -\frac{\partial \bar{p}}{\partial x_i} + \frac{\partial}{\partial x_j}\left(\frac{1}{\mathrm{Re}} + \gamma\nu_t\right)2S_{ij}^n - 2\epsilon_{i3k}\Omega\bar{u}_k + (1-\delta_{i3})\frac{\partial}{\partial z}\nu_T\frac{\partial\langle\bar{u}_i\rangle}{\partial z} - \frac{\theta'}{\theta_0}g_i, \tag{10}$$

$$\frac{\partial \bar{\theta}}{\partial t} + \bar{u}_j \frac{\partial \bar{\theta}}{\partial x_j} = \frac{\partial}{\partial x_j}\left(\frac{1}{\mathrm{Pe}} + \frac{\gamma\nu_t}{Pr_t}\right)\frac{\partial\bar{\theta}}{\partial x_j} + \frac{\partial}{\partial z}\nu_T\frac{\partial\langle\bar{\theta}\rangle}{\partial z}. \tag{11}$$

The transport equation for the SGS TKE equation [5] is:

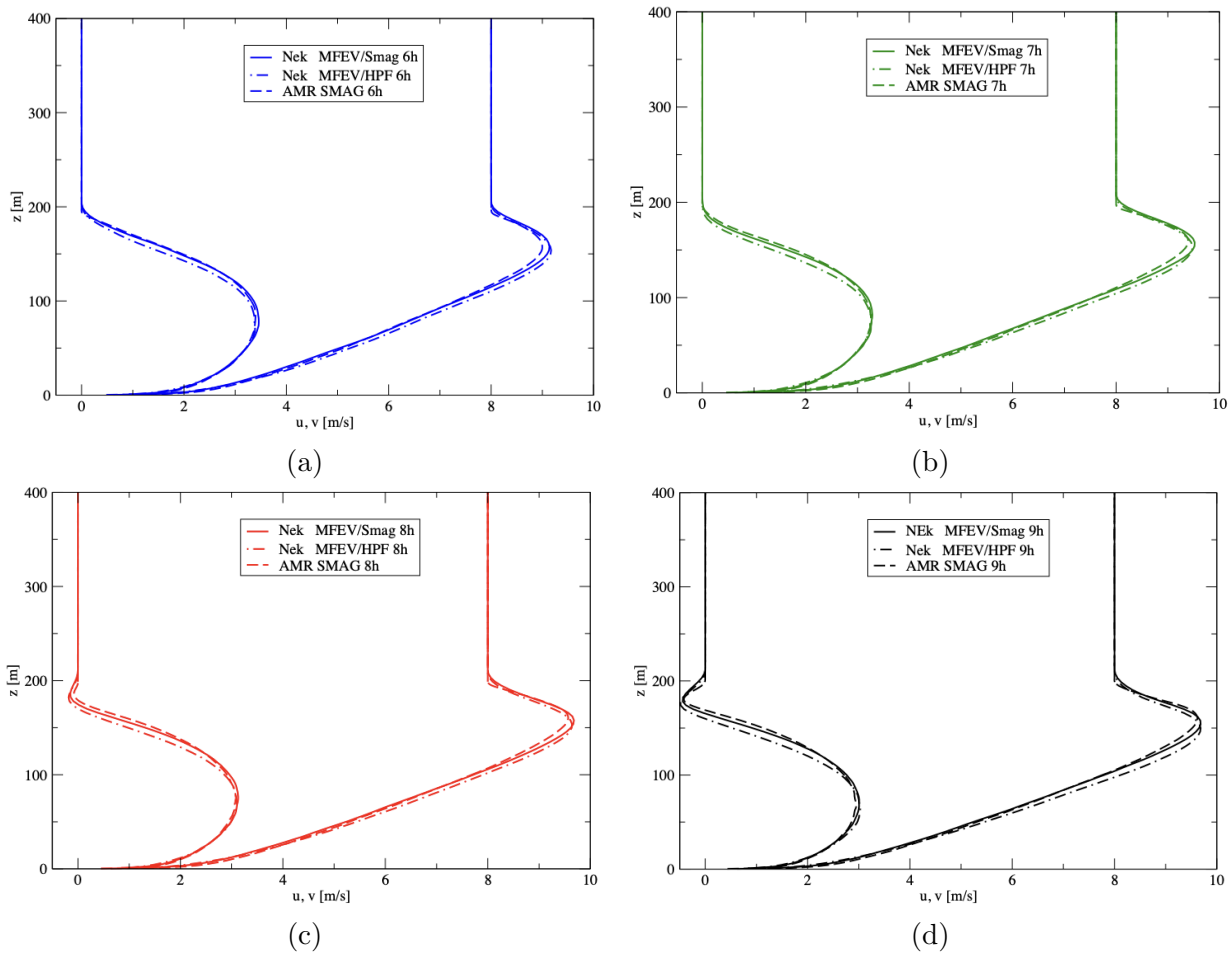

Figure 5: Mean velocity profiles from Nek5000 MEFV+HPF, MFEV+SMG, and AMR-Wind SMG at (a) $t = 6$ h, (b) $t = 7$ h, (c) $t = 8$ h, and (d) $t = 9$ h.

$$\left(\frac{\partial}{\partial t} + u_j \frac{\partial}{\partial x_j}\right) e = 2\gamma\nu_t S'_{ij} S'_{ij} + \frac{g}{\theta_0}\tau_{\theta w} - C_\varepsilon \frac{e^{3/2}}{L} + \frac{\partial}{\partial x_i}\left(\frac{1}{\mathrm{Re}} + 2\gamma\nu_t\right)\frac{\partial e}{\partial x_i} \tag{12}$$

and the fluctuating eddy viscosity, ν_t, is given by

$$\nu_t = C_k L e^{1/2}.$$

For unstable stratification, the length scale L in this equation becomes

$$L = L_{SMG} = \Delta,$$

where Δ is the cube-root of the cell volume. For stable stratification, L is reduced as suggested

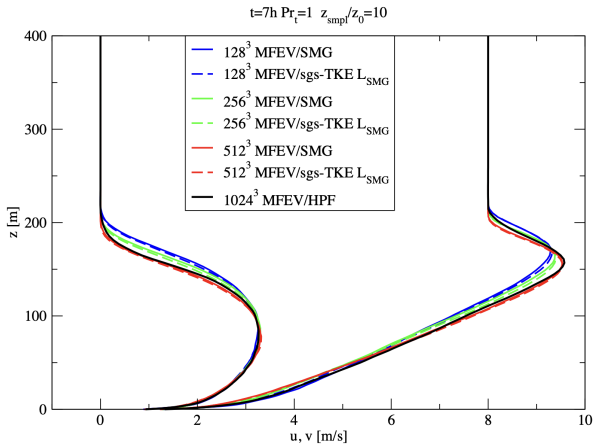

Figure 6: Nek5000 Convergence: MEFV+SMG and MFEV+HPF.

by [21] and is obtained by the following expression

$$L = L_{DRD} = \frac{0.76e^{1/2}}{\left(\frac{g}{\theta_0}\frac{\partial\theta}{\partial z}\right)^{1/2}}.$$

The definition of $\tau_{\theta w}$ is

$$\tau_{\theta w} = -\nu_\theta \frac{\partial\theta}{\partial z},$$

whereas

$$C_\varepsilon = 0.19 + 0.74L/\Delta,$$

and S'_{ij} is given by

$$S'_{ij} = S_{ij} - \langle S_{ij}\rangle .$$

The Smagorinsky constant C_s is written in terms of C_k and C_ε

$$C_s = \left(C_k\sqrt{\frac{C_k}{C_\varepsilon}}\right)^{1/2}.$$

From [5], the SGS constants are $C_k = 0.1$, and for the case where $L = L_{SMG} = \Delta$, $C_\varepsilon = 0.93$. The isotropy factor γ is obtained from

$$\gamma = \frac{S'}{S' + \langle S\rangle}, \tag{13}$$

where

$$\langle S\rangle = \sqrt{2\,\langle S_{ij}\rangle\,\langle S_{ij}\rangle}, \tag{14}$$

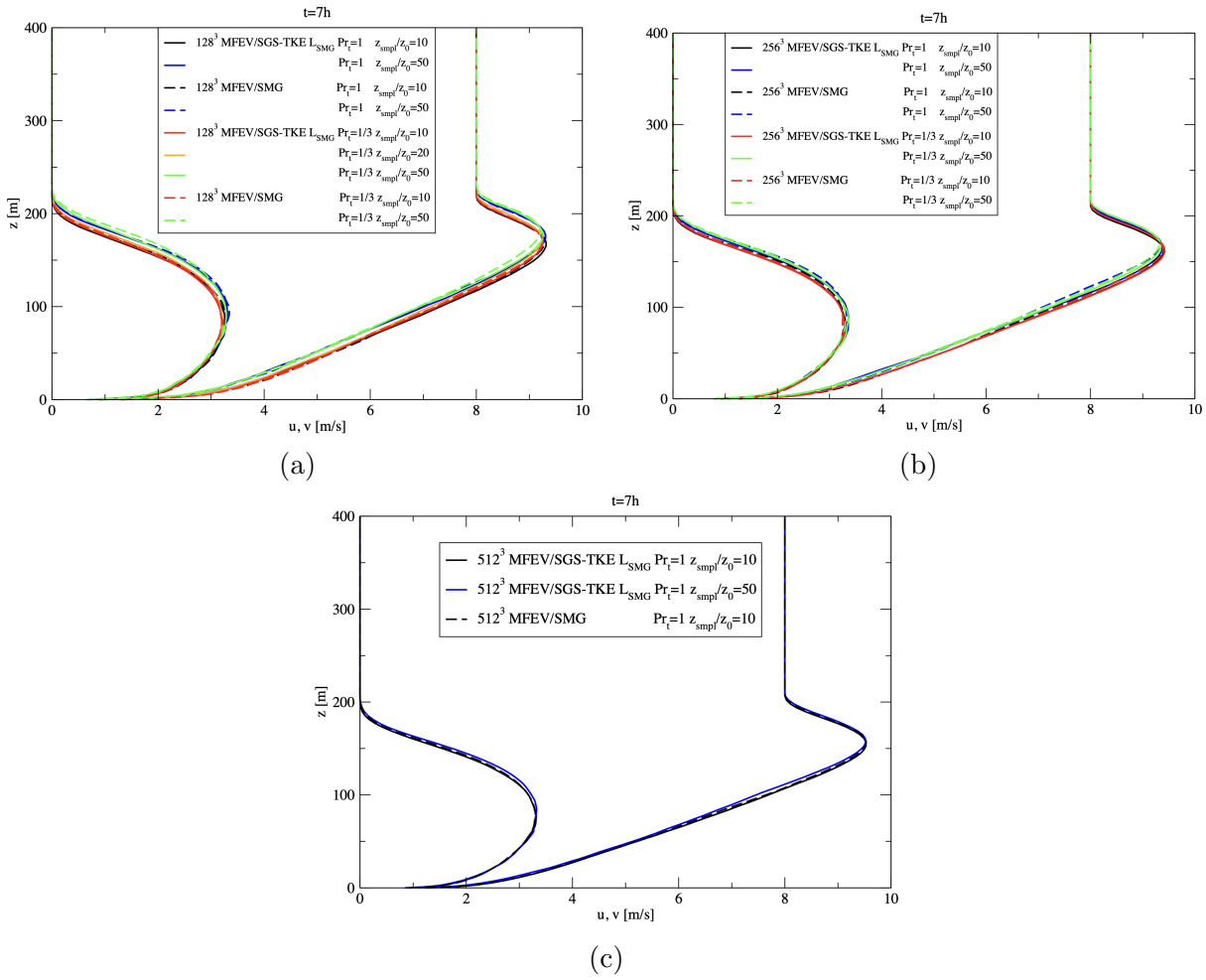

Figure 7: Effect of sampling location: horizontally averaged streamwise and spanwise velocity profiles at $t = 7$ h using z_{smpl}/z_0 values between 10 and 50 for resolutions (a) $n = 128^3$, (b) $n = 256^3$, and (c) $n = 512^3$.

and

$$S' = \sqrt{2\left\langle S'_{ij} S'_{ij} \right\rangle}. \tag{15}$$

The expression for the MFEV ν_T is derived so that the law-of-the-wall behavior can be recovered in the absence of any resolved turbulence as explained below. According to [5], a model consistent with this idea is as follows:

$$\nu_T = (C_K L_m)^2 \sqrt{2 \left\langle S_{ij} \right\rangle \left\langle S_{ij} \right\rangle}, \tag{16}$$

where S_{ij} is the strain rate tensor, C_K is a constant, and $C_K L_m$ is a mixing-length scale. Equation (16)

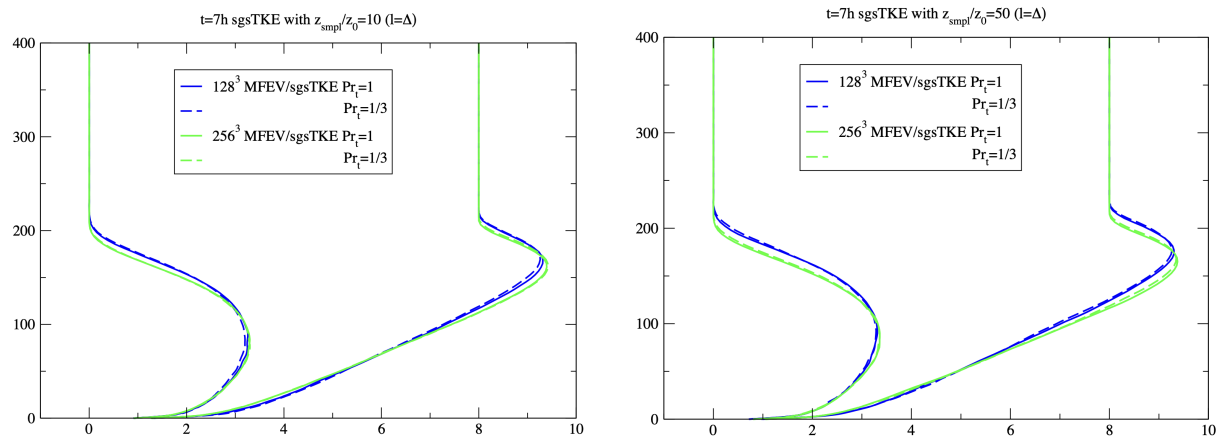

(a) (b)

Figure 8: Effect of Pr_t: horizontally averaged streamwise and spanwise velocity profiles at $t = 7$ h at resolutions 128^3, and 256^3, using (a) $z_{smpl}/z_0 = 10$ and (b) $z_{smpl}/z_0 = 50$, with Pr_t taking values 1 and 1/3.

simplifies to

$$\nu_T = (C_K L_m)^2 \sqrt{\left(\frac{\partial\langle u\rangle}{\partial z}\right)^2 + \left(\frac{\partial\langle v\rangle}{\partial z}\right)^2}, \tag{17}$$

and ignoring the mean wind turning with height at the first grid point implies that the wind-speed derivative is:

$$\sqrt{\left(\frac{\partial\langle u\rangle}{\partial z}\right)^2 + \left(\frac{\partial\langle v\rangle}{\partial z}\right)^2} \approx \frac{\partial U_s}{\partial z}, \tag{18}$$

where U_s is the average surface layer wind speed (i.e., $U_s = \left\langle\sqrt{u^2+v^2}\right\rangle$). The choice of $C_K L_m$ is guided by the need to match Monin-Obukhov similarity theory in the wall region and the expression. In this theory, the wind-speed derivative becomes

$$\frac{\partial U_s}{\partial z} = \frac{u_\tau \phi_m}{\kappa z}, \tag{19}$$

where u_τ is the friction velocity, κ is the von Karman constant, and ϕ_m is the Monin-Obukhov stability function for momentum. Following [5], in order to make use of Eq. (16) we further impose a "constant flux," traction-type boundary condition at $z = z_1$, which states that the sum of the SGS and resolved momentum fluxes be equal to the surface stress, i.e.,

$$\left[\langle\tau_{uw}^{sgs}\rangle^2 + \langle\tau_{vw}^{sgs}\rangle^2\right]^{1/2} + \left[\langle uw\rangle^2 + \langle vw\rangle^2\right]^{1/2} = u_\tau^2. \tag{20}$$

As described in [4], this traction boundary condition in Nek is imposed at the first grid point in the vertical direction, which is assumed to be a point inside the log-layer at a location $z = z_1$, where the boundary condition for the vertical velocity component is defined to be zero. For this reason the

second term in Eq. (20) corresponding to the resolved momentum fluxes is identically equal to zero. In [5], a predictive relationship for the MFEV at the first grid point z_1, $\nu_T^\star = \nu_T(z_1)$, is obtained by invoking the approximation that the fluctuating components of strain are neglected compared to the mean strain so that only the horizontally averaged SGS stress in Eq. (8) is retained. This leads to

$$\begin{aligned} \langle \tau_{uw}^{sgs} \rangle &= -\nu_T \frac{\partial \langle u \rangle}{\partial z}, \\ \langle \tau_{vw}^{sgs} \rangle &= -\nu_T \frac{\partial \langle v \rangle}{\partial z}. \end{aligned} \tag{21}$$

Upon substitution of Eq. (21) into Eq. (20) and making use of Eqs. (18) and (19), the expression for the MFEV, $\nu_T^\star$, for Nek becomes

$$\nu_T^\star = \frac{u_\tau \kappa z_1}{\phi_m\left(z_1\right)}. \tag{22}$$

Equation (22) provides an adaptive method for estimating the MFEV needed to force the computed wind speed derivative to match with similarity theory at $z = z_1$. At any other height, similar to [5], we use

$$\nu_T = \nu_T^\star \frac{\kappa z_1}{u_\tau \phi_m\left(z_1\right)} \sqrt{2 \left\langle S_{ij} \right\rangle \left\langle S_{ij} \right\rangle}, \tag{23}$$

which follows directly from Eqs. (16), (18), and (19). In contrast to [5], a similar correction was also applied to the SGS potential temperature field, and $\tau_{\theta z}^{sgs}$ becomes:

$$\left\langle \tau_{\theta z}^{sgs} \right\rangle = -\nu_T \frac{\partial \langle \theta \rangle}{\partial z}. \tag{24}$$

Following [17] and [18], as was already described in the previous subsection, in our approach the boundary of the computational domain is not located exactly at the wall but at a finite distance from the wall corresponding to a fixed value of $z_1^+ = z/z_0$. Strictly speaking, this implies that a boundary layer of width z_1 (corresponding to the specified value of z_1^+) should be removed from the computational domain; however, it is assumed that this width is very small at high Reynolds numbers and can be considered negligible, so that the equations can be solved in the whole domain with traction BCs prescribed on the lower boundary. Since the choice of z_1^+ is rather arbitrary, we have found that values of z_1^+ up to 10 at the target Re produce averaged results that do not differ significantly.

4 Results with MFEV/SGS-TKE

This section presents results obtained with the MFEV approach in conjunction with solving an SGS TKE equation. Figure 6 compares horizontally averaged streamwise and spanwise velocity profiles at $t = 7$ h, using MFEV/SMG and MFEV/SGS-TKE with L_{SMG} for resolutions $n = 128^3$, $n = 256^3$, and $n = 512^3$. For completeness, the MFEV/HPF profiles for $n = 1024^3$ are also shown. As can be observed, the difference between MFEV/SMG and MFEV/TKE-SMG using L_{SMG} is negligible for all resolutions.

As noted earlier, here we extended the work of the earlier report [4] by allowing for the sampling of tangential velocities and potential temperature at specified z-locations away from the lower wall in

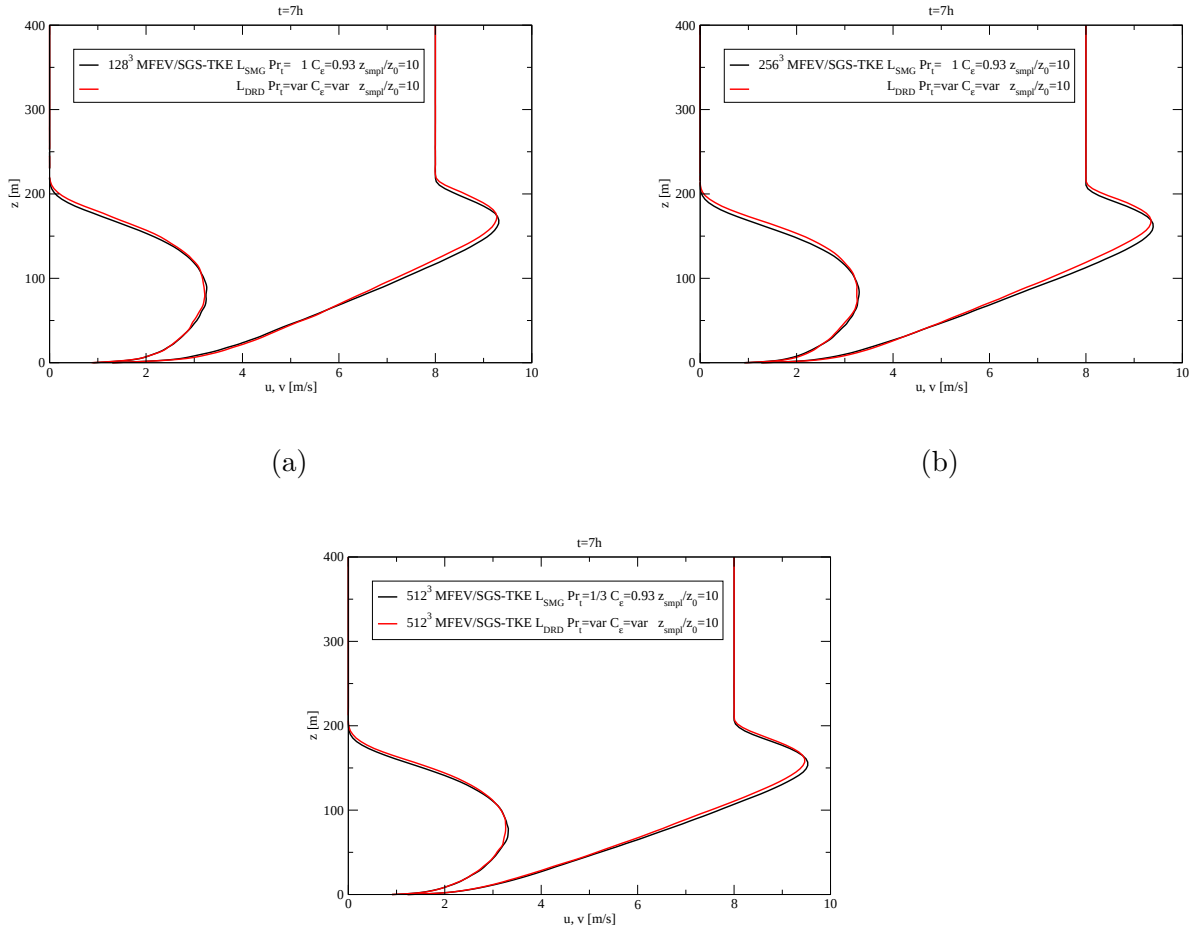

Figure 9: Effect of L_{SMG} vs L_{DRD} on horizontally averaged streamwise and spanwise velocity profiles at $t = 7$ h for resolutions (a) $n = 128^3$, (b) $n = 256^3$, and (c) $n = 512^3$ using MFEV/SGS-TKE and L_{SMG} vs L_{DRD}.

order to evaluate u_τ and θ_τ, i.e., the wall momentum and heat fluxes. The evaluation of u_τ and θ_τ is performed using the system of equations and method presented in Section 4 of [4]. To investigate the effect of the sampling location z_{smpl} on the results, simulations using MFEV/SGS-TKE with L_{SMG} were performed for various values of z_{smpl}/z_0 ranging between 10 and 50, for various resolutions. Figure 7 shows horizontally averaged streamwise and spanwise velocity profiles at $t = 7$ h using z_{smpl}/z_0 values between 10 and 50 for resolutions (a) $n = 128^3$, (b) $n = 256^3$, and (c) $n = 512^3$. An important conclusion from this study was that the effect of the sampling location diminishes with resolution, and already at $n = 512^3$ it is almost negligible.

The effect of Pr_t was also investigated for the case MFEV/SGS-TKE with L_{SMG}, and the results

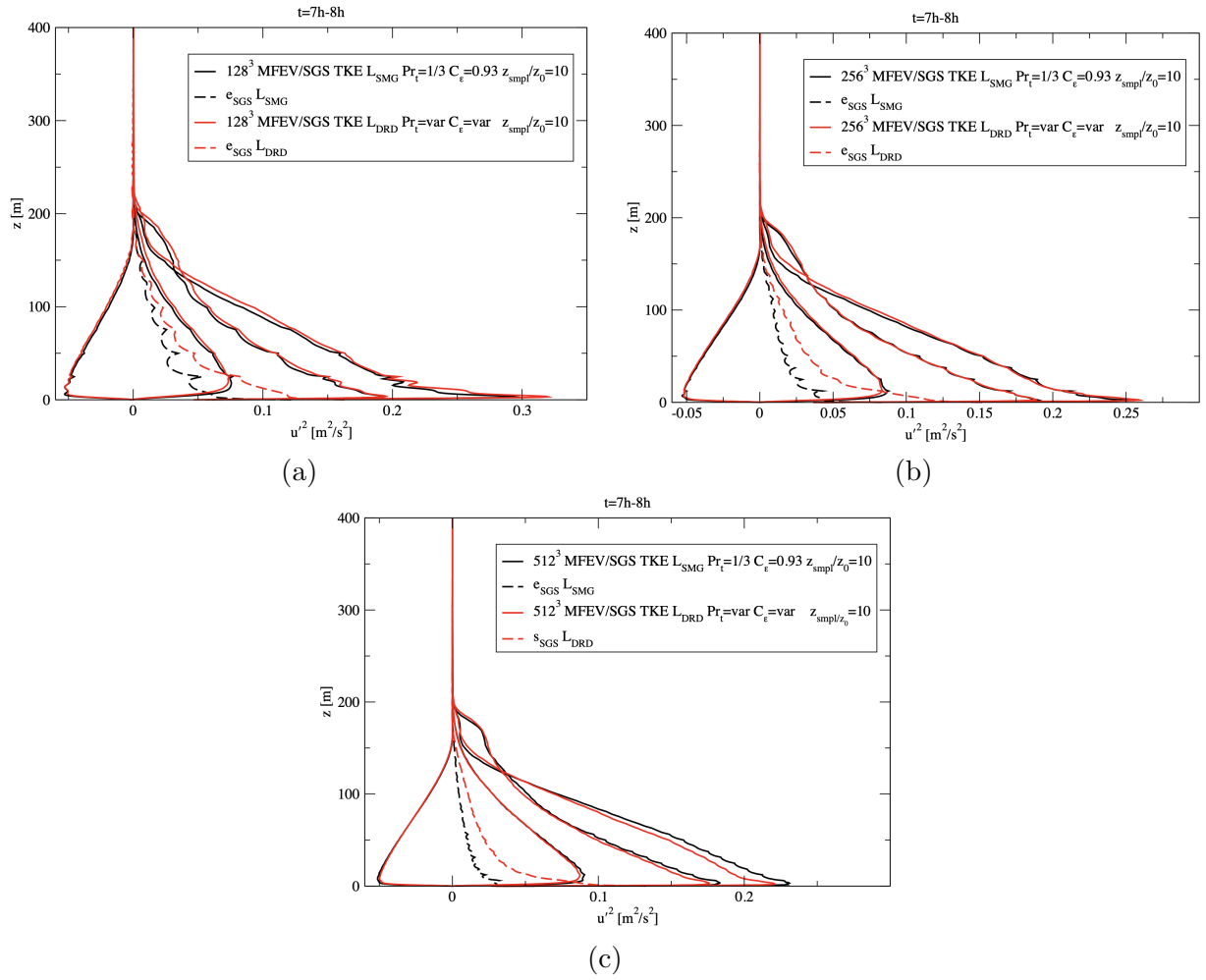

Figure 10: Effect of L_{SMG} vs. L_{DRD} on horizontally averaged streamwise, spanwise and normal fluctuation profiles at $t = 7$ h for resolutions (a) $n = 128^3$, (b) $n = 256^3$, and (c) $n = 512^3$ using MFEV/SGS-TKE and L_{SMG} vs L_{DRD}.

are shown in Fig. 8 (a) and (b) at resolutions $n = 128^3$, and $n = 256^3$, with Pr_t taking values 1 and 1/3 for $z_{smpl}/z_0 = 10$ and $z_{smpl}/z_0 = 50$, respectively. As can be observed, the effect of Pr_t is almost negligible for both resolutions studied.

A comparison of the horizontally averaged streamwise and spanwise velocity profiles at $t = 7$ h between the MFEV/SGS-TKE with L_{SMG} and the MFEV/SGS-TKE with L_{DRD} approaches is shown in Fig. 9 (a)-(c) for resolutions $n = 128^3$, $n = 256^3$, and $n = 512^3$, respectively.

A comparison of fluctuation velocities at $t = 7$ h between the MFEV/SGS-TKE with L_{SMG} and the MFEV/SGS-TKE with L_{DRD} approaches is shown in Fig. 10(a), (b), and (c) for resolutions $n = 128^3$, $n = 256^3$, and $n = 512^3$, respectively.

Figure 11 shows a comparison of the horizontally averaged streamwise and spanwise velocity profiles

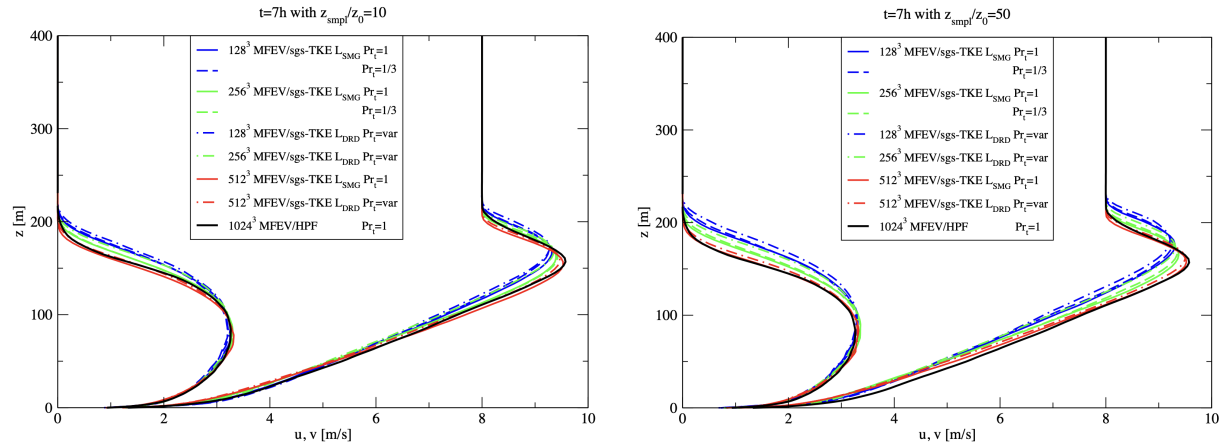

Figure 11: Horizontally averaged streamwise and spanwise velocity profiles at $t = 7$ h for resolutions $n = 128^3$, $n = 256^3$, and $n = 512^3$ using MFEV/SGS-TKE and L_{SMG} vs L_{DRD} for (a) $z_{smpl}/z_0 = 10$ and (b) $z_{smpl}/z_0 = 50$.

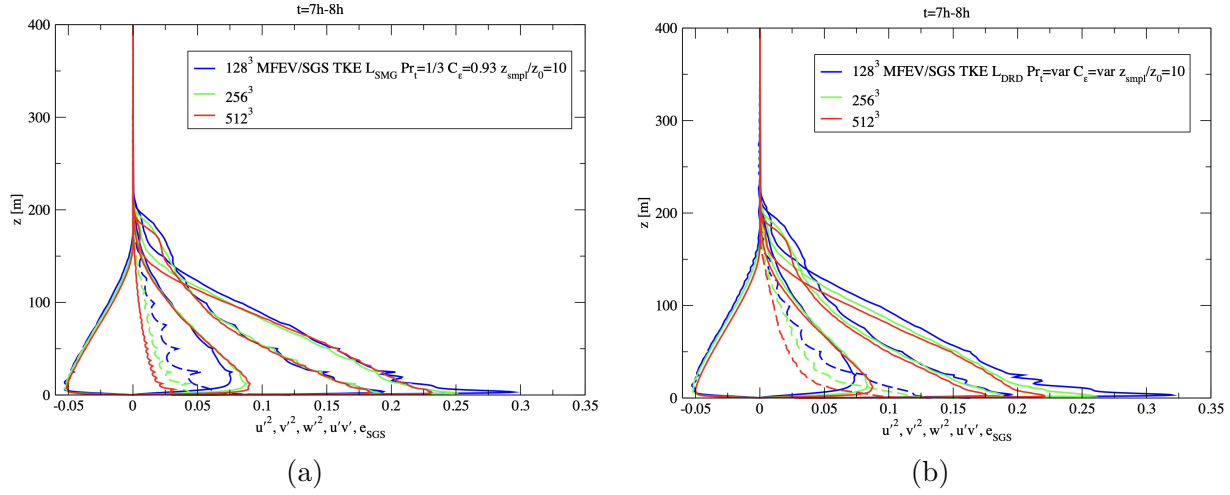

Figure 12: Horizontally averaged streamwise, spanwise, and normal fluctuation profiles at $t = 7$ h for $z_{smpl}/z_0 = 10$ using (a) MFEV/SGS-TKE with L_{SMG} and (b) MFEV/SGS-TKE with L_{DRD} for resolutions $n = 128^3$, $n = 256^3$, and $n = 512^3$.

at $t = 7$ h for (a) $z_{smpl}/z_0 = 10$ and (b) $z_{smpl}/z_0 = 50$, using MFEV/SGS-TKE with L_{SMG} and MFEV/SGS-TKE with L_{DRD} for resolutions $n = 128^3$, $n = 256^3$, and $n = 512^3$. For completeness, the MFEV/HPF profiles for $n = 1024^3$ are also shown.

Figure 12 shows a comparison of the horizontally averaged streamwise, spanwise, and normal fluctuation profiles at $t = 7$ h for $z_{smpl}/z_0 = 10$ using (a) MFEV/SGS-TKE with L_{SMG} and (b) MFEV/SGS-TKE with L_{DRD} for resolutions $n = 128^3$, $n = 256^3$, and $n = 512^3$.

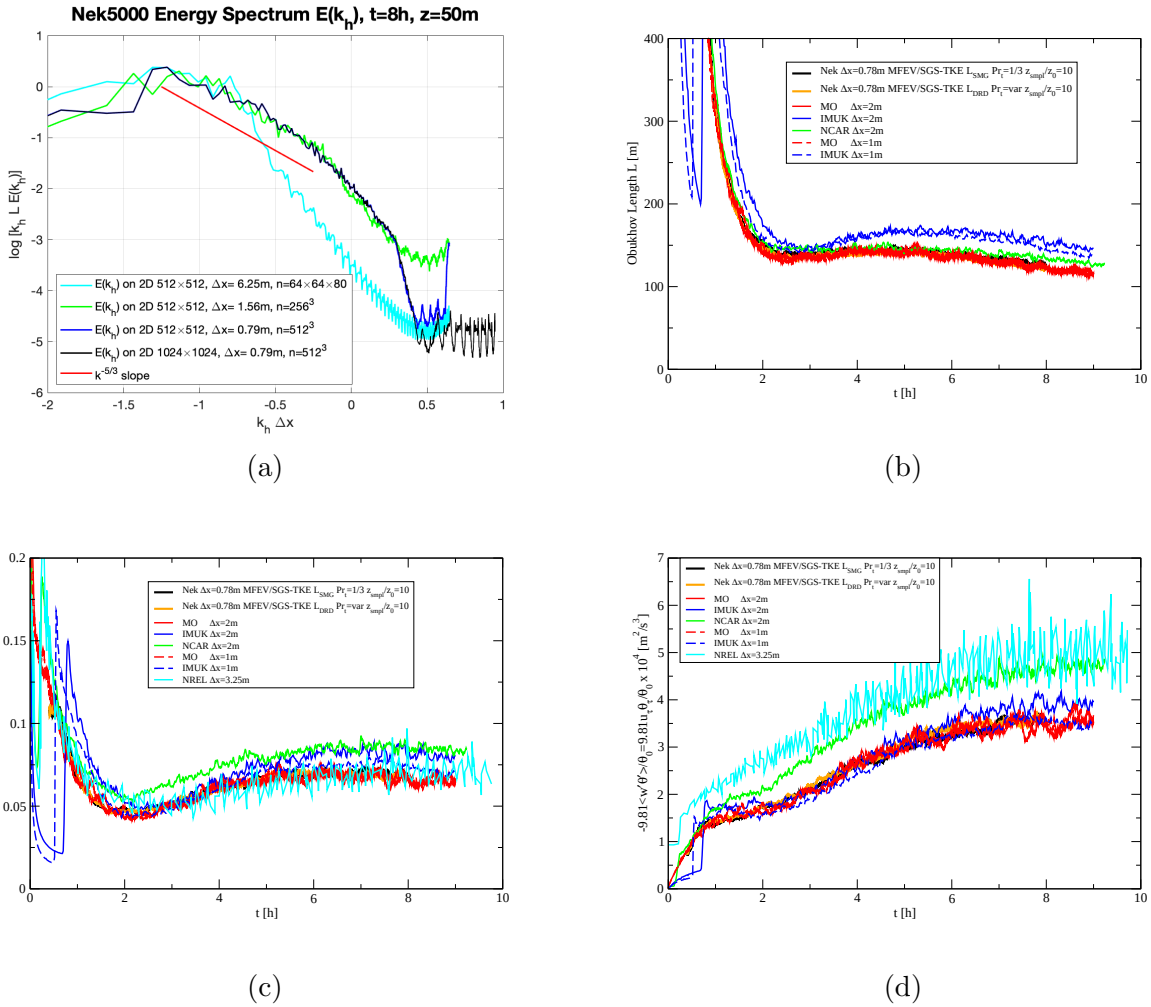

Figure 13: Nek5000 (a) spatial spectrum and time history of (b) Obukhov length, (c) momentum, and (d) temperature fluxes.

Good convergence is also observed in second-order quantities in Fig. 12 (a) and (b), for MFEV/SGS-TKE with (a) L_{SMG} and with (b) L_{DRD}. This is especially the case for resolutions $n = 256^3$ and $n = 512^3$ and for L_{SMG}. The resolved fluctuations obtained by the two approaches MFEV/SGS-TKE with L_{SMG} and L_{DRD} compare reasonably well for the same effective resolution.

Figure 13 (top left) demonstrates the spatial spectrum for velocity magnitude at $t = 6$ h for $n = 256^3$ and $n = 512^3$ resolutions. We see that both the $n = 512^3$ and $n = 1024^3$ results exhibit $k^{-\frac{5}{3}}$ energy spectrum, as expected for resolved turbulent flow simulations. The remaining figures show the comparison of Nek5000/RS to the NCAR, IMUK, and MO results for the Monin-Obukhov length, the surface momentum flux, and the surface heat flux.

5 Conclusion

We presented high-fidelity LES turbulence models for the atmospheric boundary layer flows. We considered the GABLS1 benchmark problem and extend the range of our SGS modeling approaches in the context of the mean-field eddy viscosity provided with cross-verification and validation of two different codes, Nek5000/RS and AMR-Wind, that are based on unstructured high-order and structured low-order discretizations.

Acknowledgments

This research was supported in part by the Exascale Computing Project (17-SC-20-SC), a joint project of the U.S. Department of Energy Office of Science and the National Nuclear Security Administration, responsible for delivering a capable exascale ecosystem, including software, applications, and hardware technology, to support the nation's exascale computing imperative. Funding was also provided by the U.S. Department of Energy, Office of Energy Efficiency and Renewable Energy, Wind Energy Technologies Office. This work was authored in part by the National Renewable Energy Laboratory, operated by Alliance for Sustainable Energy, LLC, for the U.S. Department of Energy (DOE) under Contract No. DE-AC36-08GO28308. We gratefully acknowledge the computing resources provided on Bebop, a high-performance computing cluster operated by the Laboratory Computing Resource Center (LCRC) at Argonne National Laboratory. The research also used computational resources sponsored by the DOE Office of Energy Efficiency and Renewable Energy and located at the National Renewable Energy Laboratory.

References

[1] Paul Fischer, Stefan Kerkemeier, Misun Min, Yu-Hsiang Lan, Malachi Phillips, Thilina Rathnayake, Elia Merzari, Ananias Tomboulides, Ali Karakus, Noel Chalmers, and Tim Warburton. Nekrs, a gpu-accelerated spectral element navier-stokes solver. *CoRR*, abs/2104.05829, 2021.

[2] Misun Min, Yu-Hsiang Lan, P. Fischer, E. Merzari, S. Kerkemeier, , M. Phillips, T. Rathnayake, A. Novak, D. Gaston, N. Chalmers, and T. Warburton. Optimization of full-core reactor simulations on summit. *2022 International Conference for High Performance Computing, Networking, Storage, and Analysis*, pages 1–11, 2022.

[3] Elia Merzaria, Steven Hamilton, Thomas Evans, Paul Romano, Paul Fischer, Misun Min, Stefan Kerkemeier, Yu-Hsiang Lan, Jun Fang, Malachi Phillips, Thilina Rathnayake, Elliott Biondo, Katherine Royston, Noel Chalmers, and Tim Warburton. Exascale multiphysics nuclear reactor simulations for advanced designs. *2023 International Conference for High Performance Computing, Networking, Storage, and Analysis*, 2023. Gordon Bell Finalist.

[4] Misun Min and Ananias Tomboulides. Simulating atmospheric boundary layer turbulence with nek5000/rs. Technical Report ANL-22/79, Argonne National Laboratory, 2022.

[5] P. Sullivan, J. McWilliams, and C.H. Moeng. A subgrid-scale model for large-eddy simulation of planetary boundary-layer flows. *Bound.-Layer Meteor.*, 71:247–276, 1994.

[6] Misun Min, Michael Brazell, Ananias Tomboulides, Matthew Churchfield, Paul Fischer, and Michael Sprague. Towards exascale for wind energy simulations. revision, 2023.

[7] C.-H. Moeng. A large-eddy-simulation model for the study of planetary boundary-layer turbulence. *Journal of the Atmospheric Sciences*, 41(13):2052–2062, 1984.

[8] P.P. Sullivan, J.B. Edson, T. Hristov, and J.C. McWilliams. Large-eddy simulations and observations of atmospheric marine boundary layers above nonequilibrium surface waves. *Journal of the Atmospheric Sciences*, 65(4):1225–1245, 2008.

[9] M.J. Churchfield and P.J. Moriarty. Modeling and simulation of wind-farm flows. In *Wind Energy Modeling and Simulation: Volume 1: Atmosphere and Plant*, pages 217–271. Inst. Eng. and Tech., 2020.

[10] Robert J Beare, Malcolm K Macvean, Albert AM Holtslag, Joan Cuxart, Igor Esau, Jean-Christophe Golaz, Maria A Jimenez, Marat Khairoutdinov, Branko Kosovic, David Lewellen, et al. An intercomparison of large-eddy simulations of the stable boundary layer. *Boundary-Layer Meteorology*, 118(2):247–272, 2006.

[11] Javier Rodrigo, Matthew Churchfield, and Brank Kosovic. A methodology for the design and testing of atmospheric boundary layer models for wind energy applications. *Wind Energ. Sci.*, 2:23–54, 2017.

[12] M.O. Deville, P.F. Fischer, and E.H. Mund. *High-order methods for incompressible fluid flow*. Cambridge University Press, Cambridge, 2002.

[13] P. Fischer, J. Lottes, and S. Kerkemeier. Nek5000: Open source spectral element CFD solver. http://nek5000.mcs.anl.gov and https://github.com/nek5000/nek5000. 2008.

[14] Center for Efficient Exascale Discretizations, Exascale Computing Project, DOE. ceed.exascaleproject.org.

[15] R.J. Beare and et. al. An intercomparison of large-eddy simulations of the stable boundary layer. *Boundary-Layer Meteorology*, (118):247–272, 2006.

[16] A. S. Monin and A. M. Obukhov. Basic laws of turbulent mixing in the surface layer of the atmosphere. *Tr. Akad. Nauk. SSSR Geophiz. Inst.*, 24(151):163—-187, 1954.

[17] H. Grotjans and F. Menter. Wall functions for general application cfd codes. In *ECCOMAS 98, Proceedings of the 4th European Computational Fluid Dynamics Conference, John Wiley & Sons*, pages 1112–1112, 1998.

[18] D. Kuzmin, O. Mierka, and S. Turek. On the implementation of the Î°-Îµ turbulence model in incompressible flow solvers based on a finite element discretisation. *International Journal of Computing Science and Mathematics*, 1(2-4):193–206, 2007.

[19] U. Schumann. Subgrid scale model for finite difference simulations of turbulent flows in plane channels and annuli. *Journal of Computational Physics*, 18(4):376–404, 1975.

[20] U. Schumann. Subgrid scale model for finite difference simulations of turbulent flows in plane channels and annuli. *Journal of Computational Physics*, (18):376–404, 1975.

[21] J. W. Deardorff. Stratocumulus-capped mixed layers derived from a three-dimensional model. *Bound.-Layer Meteor.*, 18:495–527, 1980.

Mathematics and Computer Science
Argonne National Laboratory
9700 South Cass Avenue, Bldg. 240
Lemont, IL 60439

www.anl.gov

Argonne National Laboratory is a U.S. Department of Energy laboratory managed by UChicago Argonne, LLC